Atmospheric observations with E-band microwave links – challenges and opportunities

Martin Fencl[1], Michal Dohnal[1], Pavel Valtr[2], Martin Grabner[3], Vojtěch Bareš[1]

[1]Department of Hydraulics and Hydrology, Czech Technical University in Prague, Prague 6, 166 29, Czech Republic
[2]Department of Electromagnetic Field, Czech Technical University in Prague, Prague 6, 166 29, Czech Republic
[3]Department of Frequency Engineering, Czech Metrology Institute, Brno, 638 00, Czech Republic

Correspondence to: Martin Fencl (martin.fencl@cvut.cz)

Abstract. Opportunistic sensing of rainfall and water vapor using commercial microwave links operated within cellular networks was conceived more than a decade ago. It has since been further investigated in numerous studies predominantly concentrating on the frequency region of 15–40 GHz. This manuscript provides the first evaluation of rainfall and water vapor sensing with microwave links operating at an E-band (specifically, 71–76 GHz and 81–86 GHz), which are increasingly updating, and frequently replacing, older communication infrastructure. Attenuation-rainfall relations are investigated theoretically on drop size distribution data. Furthermore, quantitative rainfall estimates from six microwave links, operated within cellular backhaul, are compared with observed rainfall intensities. Finally, the capability to detect water vapor is demonstrated on the longest microwave link measuring 4.86 km in path length. The results show that E-band microwave links are markedly more sensitive to rainfall than devices operating in the 15–40 GHz range and are thus able to observe even light rainfalls, a feat practically impossible to achieve previously. The E-band links are, however, substantially more affected by errors related to variable drop size distribution. Water vapor retrieval might be possible from long E-band microwave links, nevertheless, the efficient separation of gaseous attenuation from other signal losses will be challenging in practice.

1 Introduction

Electromagnetic (EM) waves in the microwave region are attenuated by water vapor, oxygen, fog, or raindrops. Measurements of microwave attenuation at different frequency bands thus represent an invaluable source of information regarding the atmosphere. Passive and active microwave systems have become an integral part of Earth observing satellites, terrestrial remote sensing systems, and complete remote sensing methods in other spectral regions (Woodhouse, 2017). The microwave region is, however, also increasingly utilized in communication systems allowing for new possibilities to observe atmosphere with unintentional (opportunistic) sensing. Commercial microwave links (CMLs) are an excellent example of a communication system capable of providing close-to-ground observations of the atmosphere. CMLs are point-to-point line-of-sight radio connections widely used in mobile phone backhaul for connecting hops of different lengths typically ranging from tens of meters to several kilometers. There were about 4 million CMLs operated worldwide within cellular backhaul in 2016 (Ericsson,

2016) and about 5 million in 2018 (Ericsson, 2018). Most of these CMLs operate at frequencies between 15 and 40 GHz (Ericsson, 2016, 2018) where raindrops and, to a lesser extent, water vapor represent a significant source of attenuation (Atlas and Ulbrich, 1977; Liebe et al., 1993). Information on the attenuation of any CML within countrywide networks is virtually accessible in real-time with a delay of several seconds from a remote location, typically a network operation center (Chwala

35   et al., 2016) creating an appealing opportunistic sensing system capable of providing close-to-ground observations of rainfall intensity (Leijnse et al., 2007; Messer et al., 2006) and water vapor density (David et al., 2009).

CML rainfall retrieval methods developed over the last decade have been predominantly designed and tested for frequency bands between 15 and 40 GHz (Chwala and Kunstmann, 2019). Attenuation caused by raindrops is, in this frequency region, almost linearly related to rainfall intensity and does not strongly depend on drop size distribution (DSD) (Berne and Uijlenhoet,

40   2007). Water vapor retrieval has been proposed for CMLs operating around 22 GHz (David et al., 2009) where there is a resonance line of water vapor. Increasing demands on data transfers force operators to utilize higher frequency spectra and a new generation of E-band CMLs, operating at the 71 - 86 GHz frequency band, is gradually modernizing cellular backhaul networks, especially in cities where they often replace older devices. The share of E-band CMLs in mobile phone backhaul has already reached 20 %, *e.g.,* in Poland and the Czech Republic, and it is expected to grow in other countries as E-band

45   CMLs are considered an essential part of new 5G networks (Ericsson, 2019).

E-band CMLs should be, according to recommendations for designing CMLs (ITU-R, 2005), more sensitive to rainfall, nevertheless, the relation between rainfall intensity and attenuation is not linear. Furthermore, E-band radio waves have two to four time's shorter wave lengths and the extinction efficiency (resonance peak) is highest for smaller raindrops. The attenuation-rainfall relation is, thus, more sensitive to drop size distribution, which has been already demonstrated in several

50   propagation experiments, *e.g.,* by Hansryd et al., (2010) or Luini et al. (2018). Radiowave propagation at an E-band is also more sensitive to water vapor, which poses a challenge when separating rainfall-induced attenuation from other sources of attenuation. On the other hand, the sensitivity to water vapor might also enable its detection or even monitoring.

This manuscript provides the first evaluation of E-band CMLs as rainfall and water vapor sensors. The capabilities of E-band CMLs for weather monitoring are theoretically evaluated and demonstrated on attenuation data retrieved between August and

55   December 2018 from a six E-band CML operated within cellular backhaul of a commercial provider in Prague (T-Mobile, CZ). The ultimate goal of this investigation is to provide an overview of the challenges and opportunities related to atmospheric observations with E-band CMLs. Section 2 of the manuscript summarizes based upon previous works the principles behind retrieving atmospheric variables from CML observations, Section 3 describes the methodology and datasets used in this manuscript for the assessment of E-band CMLs, Section 4 presents the results of the case study and evaluates the effect of

60   DSD on the attenuation-rainfall relation. The results are further interpreted and discussed in Section 5 followed by the conclusions which are presented in Section 6.

2 Retrieving atmospheric variables from CMLs

2.1 Components of total observed loss

Standard CMLs are monitored for transmitted tx (dBm) and received rx (dBm) signal power and the difference between tx and rx is the total observed loss L_t (dB) which can be separated into several components:

$$L_t = L_{bf} + L_m + L_{tc} + L_{rc} - G_t - G_r, \tag{1}$$

where L_{bf} (dB) is free space loss, L_m (dB) are losses in the medium, L_{tc} (dB) and L_{rc} (dB) are losses at the transmitting and receiving antennas, and G_t (dB) and G_r (dB) are antenna directive gains (Internationale Fernmelde-Union, 2009). Free space loss L_{bf} is uniquely defined by the distance d (m) between the transmitter and receiver, and by wavelength λ (m):

$$L_{bf} = 20 \left(\frac{4\pi d}{\lambda} \right) \tag{2}$$

The sum of antenna losses and gains is given by their hardware and includes interference with the environment close to antennas as antenna loss can change, *e.g.*, due to the wetness of antenna radomes. The propagation mechanisms influencing loss in the medium L_m consist of attenuation due to atmospheric gases including water vapor, which is usually not exceeding 1.5 dB km^{-1} (section 2.2), attenuation due to precipitation, which can reach several tens of dB km^{-1} (section 2.3), attenuation due to obstacles in the wave path, and diffraction losses causing bending of the direct wave towards the ground. Total loss can also be influenced by so-called multipath interference occurring due to the constructive or destructive phase summation of the signal at the receiving antenna during the atmospheric multipath propagation conditions (Valtr et al., 2011).

The separation of attenuation due to rainfall and due to water vapor from other sources of attenuation, is possible to some extent, but, firstly, dry and wet weather periods need to be identified (Overeem et al., 2011; Schleiss and Berne, 2010). Attenuation during dry weather is assumed to be a baseline, and the difference between dry and wet weather attenuation is then attributed to rainfall. Fluctuations in the baseline during dry weather can be attributed to water vapor, nevertheless, they can also be caused by temperature changes, hardware instability, etc.

The correct estimation of raindrop path attenuation and water vapor attenuation also requires the separation of additional attenuation caused by antenna radome wetting, so-called wet antenna attenuation (WAA) (section 2.4). This is especially important for shorter CMLs which are attenuated by raindrops along the short path and the relative importance of WAA contribution is significant.

2.2 Attenuation by atmospheric gasses

Attenuation by atmospheric gasses is caused predominantly by the interaction of an EM wave with molecules of water and oxygen. The evaluation of gas attenuation, as described in ITU-R (2019) and originally in Liebe et al. (1993), is based on the concept of the complex refractive index. In a medium with complex refractive index n, the intensity of EM wave I (W m^{-2}) is attenuated at distance x (m) as:

$$I(x) = I(0) \exp(-2\kappa \, Im(n) \, x),\tag{3}$$

where $\kappa = 2\pi f / c$ (m) is a vacuum wave number, c (m s^{-1}) speed of light and $Im(n)$ denotes the imaginary part of n. After introducing complex refractivity $N = (n-1)10^6$, the specific attenuation k (dB km^{-1}) is obtained as:

$$95 \quad k = 10 \, log_{10}\left(\frac{I(0)}{I(1)}\right) = 0.1819 \, f \, Im(N),\tag{4}$$

where f (GHz) is the EM wave frequency.

The attenuation due to water vapor is in here defined as the difference between wet-air and dry-air attenuation under the same moist-air pressure and temperature. Thus also effect of water vapor on dry-air attenuation is considered (ITU-R, 2019): First, dry-air pressure decreases during humid conditions (under the assumption of constant moist-air pressure) and second, partial water pressure affects the rate of collisions between the molecules (pressure broadening). Figure 1 shows specific attenuation by water vapor and dry air. Attenuation due to water vapor increases as the frequency increases, with the exception of the peak around 22 GHz and the depression around 60 GHz (Fig. 1a). The sensitivity of water vapor attenuation to temperature and air pressure monotonically increases as the frequency increases. The temperature and pressure also influence dry-air attenuation, especially at frequencies around 60 GHz (Fig. 1b).
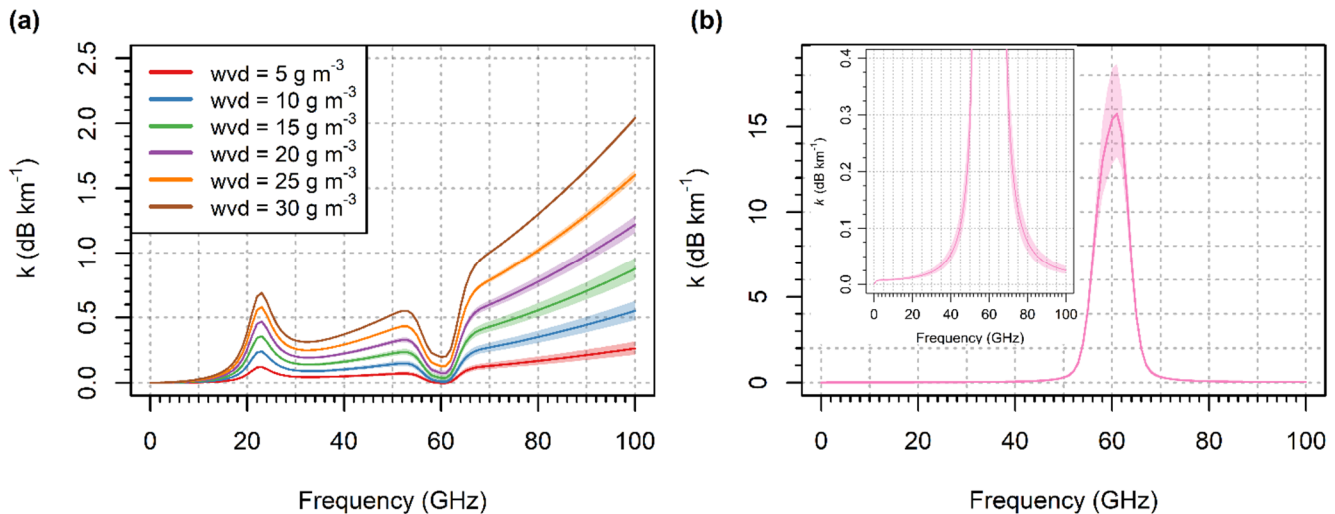
Figure 1: (a) Attenuation of EM by water vapor for frequencies 0 to 100 GHz. The relation is shown for different water vapor densities (wvd) for temperatures -10° to +30° C and pressure 1000 to 1030 hPa (colored bands). (b) Dry air attenuation of EM for temperatures -10° to +30° C and pressure 1000 to 1030 hPa (total spread represented by colored bands), inset: a detailed view of the lower attenuations.

2.3 Relation between raindrop path attenuation and rainfall intensity

Attenuation of a direct EM wave due to raindrops can be precisely calculated using the scattering theory. Attenuation caused by a single raindrop is determined by the wavelength, refractive index of water, and shape parameters of the raindrop. The extinction cross section C_{ext}, (cm^2) which can be calculated using the T-matrix method (Mishchenko and Travis, 1998),

characterizes the scattering and absorption properties of each raindrop for a given frequency and polarization. The number of drops in the unit volume per drop diameter interval $N(D)$ (m^{-3} mm^{-1}) is relatively small for natural rainfalls. Therefore, the contribution of scattered secondary EM waves radiated from particles to the incident field of the other particles is negligible. The specific raindrop path attenuation k (dB km^{-1}) can be thus considered as a sum of attenuations caused by single raindrops of diameter D (mm) and can be expressed in integral form:

$$k(f) = 4.343 \times 10^3 \int_{D_{min}}^{D_{max}} C_{ext}(D, f) N(D) \, dD, \tag{5}$$

The $N(D)$ also determines rainfall intensity R (mm h^{-1}):

$$R = 0.6 \, \pi \, 10^{-3} \int_{D_{min}}^{D_{max}} v(D) \, D^3 N(D) \, dD, \tag{6}$$

where $v(D)$ (m s^{-1}) is the terminal velocity of raindrops given by their diameters. As both specific attenuation and rainfall intensity are moments of drop size distribution (DSD), the relation between attenuation and rainfall intensity can be approximated by a power-law:

$$k = a \, R^b, \tag{7}$$

where a (mm^{-b} h^b dB km^{-1}) and b (-) are empirical parameters dependent on frequency, polarization, and DSD. When estimating rainfall from observed attenuation, Eq. (7) can be reformulated to:

$$R = \alpha \, k^\beta, \tag{8}$$

where α (mm h^{-1} dB$^{-\beta}$ km$^\beta$) $= a^{-1/b}$ and β (-) $= b^{-1}$.

The model (7) resp. (8) approximates the attenuation-rainfall relation well at frequencies around 30 GHz, nonetheless, errors increase for both lower and higher frequencies due to variable DSD (Berne and Uijlenhoet, 2007). Berne and Uijlenhoet (2007), however, investigated sensitivity to DSD only for the frequency region of 5-50 GHz. A detailed evaluation of the attenuation-rainfall model for the E-band has not been reported, yet higher sensitivity of E-band CMLs to DSD has been demonstrated during several propagation experiments (Hansryd et al., 2010; Luini et al., 2018). Furthermore, different sensitivities of E-band CMLs to DSD, compared to lower frequencies, is also obvious from their extinction efficiency:

$$Q_{ext} = \frac{C_{ext}}{\sigma_{geo}}, \tag{9}$$

where C_{ext} (cm^2) and σ_{geo} (cm^2) are extinction resp. geometric cross-sections of a raindrop. The extinction efficiency Q_{ext} of EM waves at the E-band is the highest for smaller raindrops (Fig. 2), which is characteristic for stratiform rainfalls, whereas larger raindrops characteristic for convective rainfalls (section 3.4) contribute relatively less to the total attenuation.
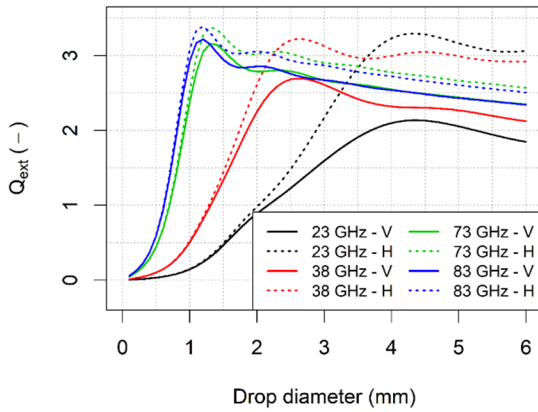
Figure 2: Extinction efficiency of plane waves at different frequencies and polarizations (H – horizontal, V – vertical).

2.4 Wet antenna attenuation

Wet antenna attenuation (WAA) is caused by a water layer forming on antenna radomes during rainfall events or dew occurrence. Modeling WAA is challenging as the formation of water film on antennas is a complex process dependent on rainfall intensity, wind direction and velocity, or air and rain temperature, as well as on antenna radome hydrophobic properties. On the other hand, WAA represents a substantial part of total attenuation (Fencl et al., 2019), especially by shorter CMLs, and its identification and separation from attenuation caused by raindrops along a CML path is crucial when obtaining reliable rainfall estimates.

Most of the models, specifically suggested for microwave link rainfall retrieval, are empirical and designed for lower frequencies (Minda and Nakamura, 2005; Overeem et al., 2011; Schleiss et al., 2013). However, the semi-empirical model suggested by Leijnse et al. (2008) enables WAA for an arbitrary frequency to be calculated. The Leijnse model assumes a layer of water with constant thickness which is assumed to be power-law related to rainfall intensity. The parameters of this relation need to be optimized. According to the Leijnse model, WAA typical of E-band CML frequencies is about two times higher than of 38 GHz. Hong et al. (2017), however, showed on 72 and 84 GHz microwave links that WAA depends highly on specific hardware settings. An antenna without radome experienced WAA of about 7 dB during a spraying experiment with artificial rain. The antenna covered by a radome (which is a typical setting of CMLs) experienced WAA of approx. 2 dB and WAA decreased further to only approx. 0.3 dB when a radome with hydrophobic coating was used. Similarly low values of WAA at E-band CMLs have been reported by Ostrometzky et al. (2018) who observed WAAs of 0.86 ± 0.54 dB and 1.07 ± 0.75 dB at two 73 GHz CMLs. These values are significantly lower than previously observed WAA at lower frequencies (Fencl et al., 2018; Minda and Nakamura, 2005; Schleiss et al., 2013), although E-band CMLs should be, in theory, more sensitive to WAA (Leijnse et al., 2008).

3   Material and Methods

The E-band evaluation concentrates on i) gaseous attenuation and its relation to water vapor density and air temperature, ii) the relation between raindrop attenuation and rainfall intensity, and iii) processing routines for separating different attenuation components. The methodology combines numerical experiments using virtual attenuation time series simulated from weather observations with analyses of CML observations obtained during the dedicated case study.

3.1 Experimental sites and instrumentation

Drop size distribution is obtained from a PARSIVEL disdrometer (1st generation, manufactured by OTT). Drop counts and fall velocities are recorded over 30 s intervals. The data was collected during the CoMMon experiment in Duebendorf (CH) at site 2, which is described, *e.g.*, in Wang et al. (2012). We further refer to this dataset as Duebendorf data.

The E-band evaluation case study is performed on six CMLs (Table 1) located in the south-east suburb of Prague (CZ). Five shorter CMLs are located in a residential area with a housing estate. The path of the long CML goes over an area with mostly agricultural land use (Fig. 3). The main node from which all CML paths originate is located on the roof of a 65-m-tall building; the end nodes are about 15 m to 30 m above ground. All the CMLs operate at an Ericsson MINILINK platform and were deployed to the site during 2016 and 2017. CMLs have full-duplex configuration with two sub-links operating in one direction at 73–74 GHz and in the second direction at 83–84 GHz with a duplex separation of 10 GHz. Transmitted signal power *tx* and received signal power *rx* are collected with custom-made server-sided software which polls selected CMLs using SNMP protocol and stores records into a PostgreSQL database. The sampling time step is approx. 10 s. The resolution of a *tx* and *rx* reading is 0.1 dBm. All devices have automatic transmitted power control (ATPC), *i.e.*, transmitted power is automatically controlled to minimize fluctuations in *rx*. CML data acquisition is described in detail in the *Supplementary material*.

Tipping bucket rain gauges (MR3, METEOSERVIS v.o.s., catch area 500 cm^2, resolution 0.1 mm) have been deployed at four measuring sites. Two rain gauges are located at the end nodes of the long CML, one at ground level close to the CML path about 1.5 km from the main network node, and one about 2 km south-west from the main node. The rain gauges at sites 1 and 2 are equipped with temperature and air humidity sensors collecting observations in a 5-min time step. All four rain gauges have been regularly maintained (on a monthly basis) and are dynamically calibrated (Humphrey et al., 1997). We further refer to the case study dataset as Prague data (Fencl et al., 2020).
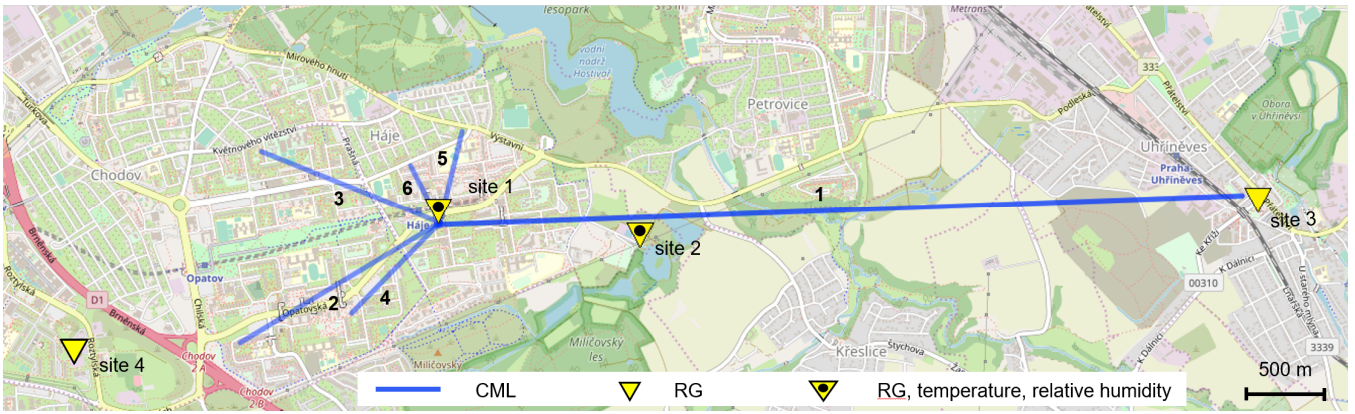
Figure 3: Case study area Prague-Haje, CZ. Two of the rain gauges are equipped with air humidity and temperature probes. ©OpenStreetMap contributors.

190

Table 1: CML characteristics in Prague-Haje, CZ. The suffixes A and B denote first, resp. second end node, and suffixes "a" and "b" the direction from A to B resp. B to A.

ID	LonA (deg)	LatA (deg)	LonB (deg)	LatB (deg)	Freq_a (GHz)	Freq_b (GHz)	Pol_a	Pol_b	Length (m)
1	14.5290	50.0301	14.5970	50.0317	73.5	83.5	V	V	4866
2	14.5291	50.0302	14.5122	50.0237	73.75	83.75	V	V	1409
3	14.5291	50.0302	14.5140	50.0341	72.75	82.75	V	V	1164
4	14.5291	50.0302	14.5216	50.0253	74.25	84.25	H	H	765
5	14.5310	50.0352	14.5291	50.0302	73	83	V	V	573
6	14.5291	50.0302	14.5266	50.0333	73.25	83.25	H	H	389

3.2 Experimental data

195 **Experimental periods:** Duebendorf data span from March 2011 to April 2012. Prague data span from 20th August to 16th December 2018. The rainfall observations are, due to technical problems available from 28th October to 16th December 2018.

Duebendorf data: The disdrometer data is quality-checked and suspicious records are excluded using filters described in Jaffrain and Berne (2010). Moreover, only records classified by the disdrometer as rainfall (at least from 90 %) are used for further analysis; hail events are excluded. The data which pass the quality check are aggregated to a 1-min temporal resolution

200 using averaging.

Prague data: Total loss is calculated for each CML as the difference between transmitted and received signal powers. The total loss data is aggregated using averaging to a 1-min temporal resolution.

Rain-gauge data are separated into rainfall events. An event is defined as a period with intervals between consecutive rain gauge tips shorter than one hour. The rainfall events with rainfall depth lower than 1 mm are excluded from the evaluation. Furthermore, events during which the temperature dropped below 2° C were also excluded from the evaluation to limit the performance assessment to liquid precipitation only. This results in a set of five events (see Table 2) representing, in terms of total depth, 81 % of all the precipitation during the experimental period. Rainfall data are aggregated by averaging to a 15-min temporal resolution to limit uncertainties due to rain gauge quantization and uncertainties related to uncaptured rainfall spatial variability. The 15-minute rainfall intensities are, for all four rain gauges, highly correlated (r = 0.88–0.96). The cumulative rainfall observed by the rain gauges is also in very good agreement and differs from the mean rainfall only by 1–3 %.

The air temperature and relative humidity data (5-min temporal resolution) are not further processed. The correlation coefficient between temperature observations is 0.95 and between humidity observations 0.86. In general, observations on the roof of the 65-m-tall building (site 1) have slightly lower variability than close-to-ground observations (site 2). The discrepancies are especially pronounced during transient conditions in the morning.

Table 2: Rainfall events used for the evaluation of CML rainfall retrieval

Event start	Duration (min)	Depth (mm)	R_{max} (mm h^{-1})
2018-10-28 01:10	1218	21.0	4.4
2018-11-02 19:14	500	5.1	2.5
2018-11-24 09:46	176	1.9	1.7
2018-12-03 05:00	158	1.8	2.6
2018-12-03 22:03	210	4.9	3.0

3.3 Gaseous attenuation

The effect of temperature and air humidity on total CML attenuation is estimated theoretically from observed air temperature and relative humidity (see section 2.2) and compared to the real CML data obtained during the case study from the long CML (ID 1). Atmospheric pressure was not measured and is assumed to be constant corresponding to average sea-level pressure. Atmospheric pressure changes related to weather conditions have, however, an almost negligible effect on theoretical attenuation (ITU-R, 2019). The temperature and air humidity used in the analyses are averages from the observations at two locations along the CML path. Gaseous attenuation is estimated for the period from 20th August to 16th December 2018 and only considers dry weather, *i.e.,* periods without rainfall and dew occurrences (events causing the tipping of at least one of the rain gauges). A safety window of 6 h was set before and after each event with an event considered to start with the first tip of any rain gauge and ending with the last tip.

The theoretical attenuation derived from air temperature and relative humidity observations is then compared to the observed attenuation of the long CML. To enable a comparison, the observed attenuation is also aggregated to a 5-min time step corresponding to the time step of temperature and humidity observations, resp. theoretical attenuation. Furthermore, the constant baseline is subtracted from the observed attenuation time series. The constant baseline is set separately for each sub-link (73.5 GHz and 83.5 GHz), such as the median attenuation obtained after the baseline separation corresponds to the median theoretical attenuation. The median attenuation is calculated considering dry-weather periods only.

The observed attenuation patterns are compared to the theoretical patterns calculated from temperature and air humidity observations assuming constant atmospheric pressure at sea level. The agreement between theoretical and observed attenuation is quantified in terms of correlations and the magnitude of their amplitudes. In addition, seasonal drift is demonstrated on time series smoothed by a moving average with a window size of one week.

Table 3: Empirical parameters of convective and stratiform rainfall for DSD reconstruction as observed by Fujiwara (1965) and re-parameterized by Ulbrich (1983).

Type	N_0 (m^{-3} cm$^{-1-\mu}$)	μ (-)	ε (h$^{-\delta}$)	δ (-)
Convective (thunderstorm)	$7.05\ 10^4$	0.4	0.118	0.20
Widespread or stratiform	$1.96\ 10^5$	0.18	0.082	0.21

Note: N_0 (m^{-3}cm$^{-1-\mu}$) and μ (-) are parameters of semi-empirical gamma distribution function, ε (h$^{-\delta}$) and δ (-) are scaling parameters of this function.

3.4 Sensitivity of the k-R model to drop size distribution

The analysis of the k-R model (Eq. 8) with respect to DSD is based on fitting Eq. (8) on attenuation and rainfall intensities obtained from Eq. (5) and (6). c First, the sensitivity of the k-R model parameters (8) to the type of rainfall (stratiform vs. convective) is investigated on theoretical DSD and secondly on real DSD from the Duebendorf dataset.

Investigation of theoretical DSD: The number of drops N with diameter D is modeled using the gamma distribution function scaled to rainfall intensity (Ulbrich, 1983). The parameters of gamma distribution for stratiform and convective rainfall are taken from Ulbrich (1983). The empirical parameters needed for the reconstruction of $N(D)$ for stratiform and convective rainfall are in Table 3. The distribution functions for two different rainfall intensities are shown in Fig. 4.

$N(D)$ is calculated for a sequence of reference rainfall intensities from 0 to 50 mm h^{-1} with an increment of 0.1 mm h^{-1} for both types of rainfalls. Specific attenuations corresponding to a given intensity and rainfall type are then calculated according to Eq. (5). Specific attenuations are calculated for 73.5 and 83.5 GHz, vertical polarization, *i.e.*, frequencies of the sub-links belonging to the long CML in the Prague data. These frequencies are approximately in the middle of the frequency bands of 71–76 GHz and 81–86 GHz allocated for E-band fixed wireless services and, thus, representative for all E-band CMLs.

The k-R model (Eq. 8) is fitted separately for each frequency and rainfall type by minimizing the sum of squared residuals between reference rainfall intensities (Eq. 6) and rainfall intensities estimated by the model using a specific attenuation obtained by Eq. (5).

Investigation of Duebendorf DSD data: The effect of DSD on the k-R power-law approximation is further tested on DSD data (Duebendorf) and its influence on rainfall estimation accuracy is quantified. The procedure is analogous to the analysis of the theoretical DSD. However, rainfall intensities and specific attenuations are calculated from the observed DSD. The rainfall records are classified into two types according to the mass-weighted drop diameter D_m (mm), which is the ratio between the fourth and third DSD moments:

$$D_m = \frac{\int_{D_{min}}^{D_{max}} N(D)D^4 dD}{\int_{D_{min}}^{D_{max}} N(D)D^3 dD} \ ,$$

(10)

The mass-weighted diameter D_m is a common descriptor of the center of a probability density function $f(D)$ characterizing DSD, thus the D_m-based classification resembles the classification on convective and stratiform rainfalls (Jaffrain and Berne, 2012). The mass-weighted diameter can be approximately related to the rainfall intensity by a power-law function:

$$\widehat{D_m} = c\,R^d,$$

(11)

where R (mm h^{-1}) is rainfall intensity and c (h^{-d} mm$^{1/d}$) and d (-) are empirical parameters. Such an approximation results in perfect fits for stratiform and convective rainfall types when applied to theoretical DSD (Fig. 4b). The approximation (Eq. 11) is used to calculate threshold for classifying disdrometer records as convective or stratiform. The threshold is dependent on rainfall intensity. Parameters c and d are estimated by fitting Eq. (11) to D_m as derived from real disdrometer data using Eq. (10).
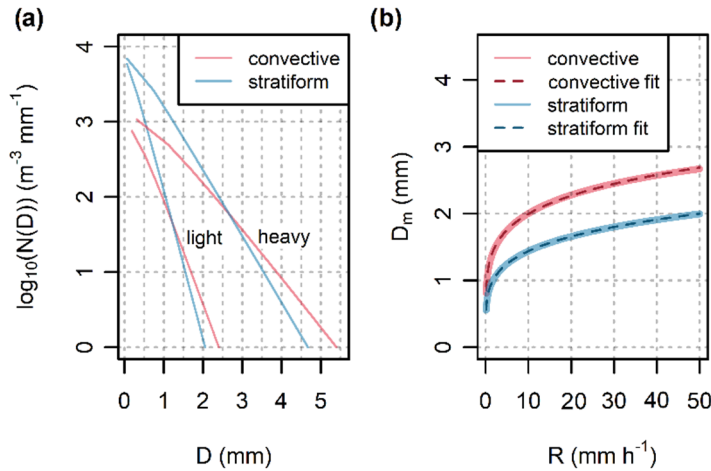
Figure 4: (a) Theoretical DSD for light (1 mm h^{-1}) and heavy (50 mm h^{-1}) convective and stratiform rainfall, and (b) the power-law relation between mass weighted diameter D_m and rainfall intensity for the same rainfall types. Gamma distribution functions with parameters corresponding to storms reported by Fujiwara (1965) are used.

Performance evaluation: The performance of k-R power-law approximation is evaluated by comparing rainfall intensities obtained directly from DSD (Eq. 6) to rainfall intensities estimated from the k-R model (Eq. 8). Virtual specific attenuations derived from DSD (Eq. 5) for two different frequencies are used as inputs to the k-R model. The performance is evaluated for three model settings: i) the k-R model with a single set of parameters obtained by fitting the model to the whole dataset, ii) the k-R model with two sets of parameters for periods with stratiform resp. convective rainfall obtained by fitting the model separately for these two rainfall types, iii) the k-R model with parameters from ITU recommendations (ITU-R, 2005).

The analysis is first evaluated for the theoretical DSD (theoretical PDFs describing drop size spectra) and secondly, in more detail, for DSD measured by a disdrometer. In the second analysis, the k-R model is evaluated in terms of root mean square error criterion (RMSE) for the whole dataset and then separately for light ($R \leq 4$ mm h^{-1}), moderate (4 mm h^{-1} < $R \leq 12$ mm h^{-1}) and heavy ($R > 12$ mm h^{-1}) rainfalls. The parameters of the k-R model obtained for Duebendorf data are verified on CML attenuation observations in Prague data.

3.5 CML rainfall retrieval

Rainfall retrieval is performed for each sub-link separately. First, total observed loss aggregated to a 1-min resolution is quality-checked. Second, total observed loss is aggregated to a 15-min temporal resolution and the baseline is identified and separated. Third, WAA is estimated and, finally, attenuation corrected for WAA is converted to rainfall intensity. Although dry-wet weather classification is not used for rainfall retrieval in this study, it is included in the *Appendix A* as it might be needed for future studies and applications (see Discussion section).

Quality check: All the time series of total losses are visually inspected to identify obvious hardware related artifacts. In one case (CML 2), the sudden change in the baseline is manually corrected, as automated procedures used for attenuation processing are not designed to cope with this artifact. Hardware-related artifacts are in more detail presented in *Appendix B*.

Baseline identification: Background attenuation, the so-called baseline, is needed to identify rainfall induced attenuation and is estimated as a moving median with a centered window having a size of one week applied on time series of total losses averaged over 15-minute intervals. A one-week window size seems to be appropriate for the climate of the Czech Republic as it covers a period with more than half of the records belonging to dry weather. On the other hand, it is sufficiently short to reliably capture long-term baseline drifts related to the instability of the CML hardware, or gaseous attenuation.

Wet antenna attenuation: WAA during rainfall is estimated by comparing attenuations as observed by sub-links of different path lengths. WAA quantification assumes spatially uniform rainfall under which specific attenuations $k_1, k_2, ..., k_n$ (dB km^{-1}) of the sub-links 1, 2, ..., n operating at the same frequency band in the same area should be identical:

$$k_1 = \frac{A_1 - Aw_1}{l_1} \approx k_2 = \frac{A_2 - Aw_2}{l_2} \approx \cdots \approx k_n = \frac{A_n - Aw_n}{l_n}, \tag{12}$$

where A (dB) is rainfall-induced attenuations, *i.e.*, the difference between total observed loss L_t and the baseline, Aw (dB) is wet antenna attenuation and l (km) is CML (sub-link) length. Assuming correct baseline identification and the same Aw for all CMLs, Aw can be directly quantified from any pair of sub-links of different lengths operating at the same frequency. The

accuracy of the quantification relies on the fulfillment of the assumptions and the difference between the sub-link lengths. The larger is the length difference between the CMLs, the smaller is the effect of an inaccurate baseline identification or dissimilar Aw within the CML pair. On the other hand, the assumption of spatially uniform rainfall is unlikely to be valid for CMLs covering a large area, *i.e.*, with contrasting lengths.

WAA is quantified at each time step by comparing the attenuation of the short CMLs to the attenuation of the long CML. WAA after rainfall and during dew events is assumed to be equal to the total attenuation. WAA evaluated for short CMLs is then related to rainfall intensity in terms of correlation. Wet antenna analysis is performed on attenuation data aggregated to 15 min.

Rainfall estimation: Rainfall is estimated for each sub-link using the k-R power-law model (Eq. 8) with ITU parameters and parameters derived from DSD classified as stratiform rains, alternatively. The parameters for stratiform rainfalls are used for its dominance in light and moderate autumn rainfalls in the Czech Republic. The specific attenuation k (dB km^{-1}) used as an input to the k-R model is calculated:

$$k = max \left(\frac{L_t - B - Aw_{const}}{l}, 0 \right), \tag{13}$$

where L_t (dB) is the total observed loss, B (dB) is the baseline, Aw_{const} (dB) is constant WAA, and l (km) is the CML, resp. sub-link path length. The constant WAA is estimated separately for 73–74 GHz and 83–84 GHz sub-links as the median of WAA values quantified according to Eq. (12).

CML rainfall retrieval performance is evaluated for two sets of k-R model parameters: parameters derived from ITU recommendations and parameters obtained from DSD observations (Duebendorf) classified as stratiform. The CML quantitative precipitation estimates (QPEs) of the long CML are compared to average 15-min rainfall from rain gauges at the sites 1, 2, and 3. The QPEs of the short CMLs are compared to average 15-min rainfall from rain gauges at the sites 1, 2, and 4. The quantitative evaluation focuses on the long CML, which is sufficiently long to capture even the light rainfalls dominating the Prague data. The performance of the short CMLs is shown to demonstrate limitations related to the improper baseline and WAA identification which are, especially during light rainfalls, more pronounced by shorter CMLs. The CML QPEs are evaluated over selected rainfall events (Table 2) in terms of correlation, relative error in cumulative rainfall, and RMSE.

4   Results

4.1 Gaseous attenuation – effect of air humidity and temperature

Theoretical gaseous attenuation calculated from observed temperatures and relative humidity is highly correlated to water vapor density (r = 0.94–0.97) at both frequencies studied. The fluctuations in temperature affect this relation negligibly. The further evaluation, therefore, concentrates on the comparison of theoretical attenuation to attenuation observed by two sub-links of the long CML 1. To separate gaseous attenuation from other possible attenuations, only periods with no rainfall are evaluated.

Time series of theoretical and observed attenuation are compared in Fig. 5 which shows time series of attenuations smoothed by a moving average (one-week window size). The correlation between theoretical and observed attenuation is high for both sub-links (r = 0.82–0.83) and the long-term patterns of observed and theoretical attenuations correspond to each other quite well. Both theoretical and observed attenuations are higher during the summer period (August-September) and gradually decrease during the autumn period (October–December). The difference between mean attenuation levels in August and December is about 1 dB for the 83.5 GHz sub-link compared to only 0.7 dB for the 73.5 GHz sub-link. The theoretical and observed attenuations have similar median values for both frequencies during summer (2.11 resp. 2.12 dB for 73.5 GHz and 2.05 resp. 2.09 dB for 83.5 GHz). The theoretical and observed attenuations during autumn are about 0.3 dB higher for 73.5 GHz, compared to the 83.5 GHz sub-link (1.81 resp. 1.93 dB for 73.5 GHz compared to 1.58 resp. 1.65 dB for 83.5 GHz). The higher attenuations of the 73.5 GHz sub-link during the autumn period, in comparison to the 83.5 GHz sub-link, can be explained by dry air attenuation. Dry air attenuation of 73.5 GHz is about 0.2 - 0.3 dB higher (depending on temperature) than that of 83.5 GHz. On the other hand, higher frequency bands are more sensitive to water vapor attenuation, which is higher during summer. Different sensitivity to water vapor attenuation also causes more significant seasonal drift in the attenuation of the 83.5 GHz sub-link compared to the 73.5 GHz one.

The discrepancies between theoretical and observed attenuations are more pronounced when analyzing data at a 5-min resolution, as demonstrated on the time series of four summer days shown in Fig. 5b. This is because the separation of gaseous attenuation from the other sources of attenuation or hardware related artifacts is challenging in real conditions. Despite these discrepancies, the correlation between theoretical and observed attenuations remains relatively high (r = 0.70–0.72). The theoretical and observed attenuations are highly correlated during August (Fig. 6) with the correlation coefficients reaching 0.84 and 0.90 for the 73.5 GHz (1a) resp. 83.5 GHz (1b) sub-link. The correlation is lowest during December (r = 0.36 resp. 0.16).
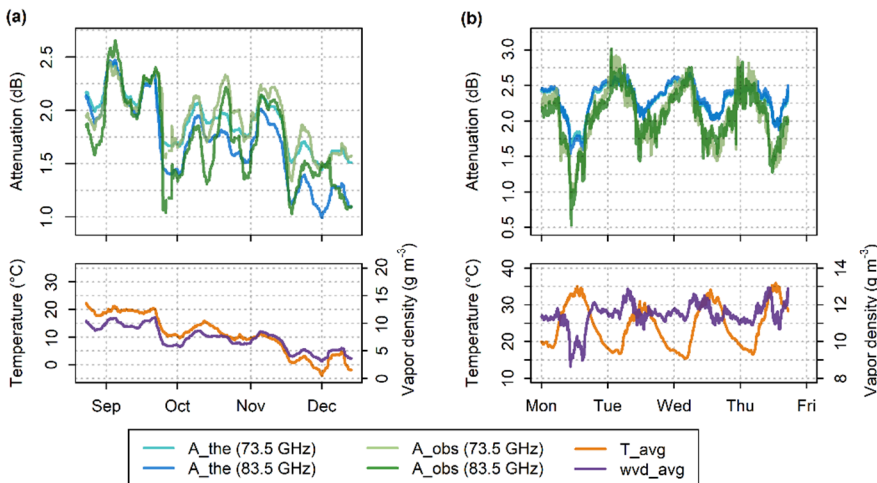
Figure 5: Theoretical and observed attenuation from the 73.5 and 83.5 GHz sub-links of CML 1 – (a) data over the whole observation period smoothed by a moving average with a window size of one week; (b) 5-min data during four summer days.
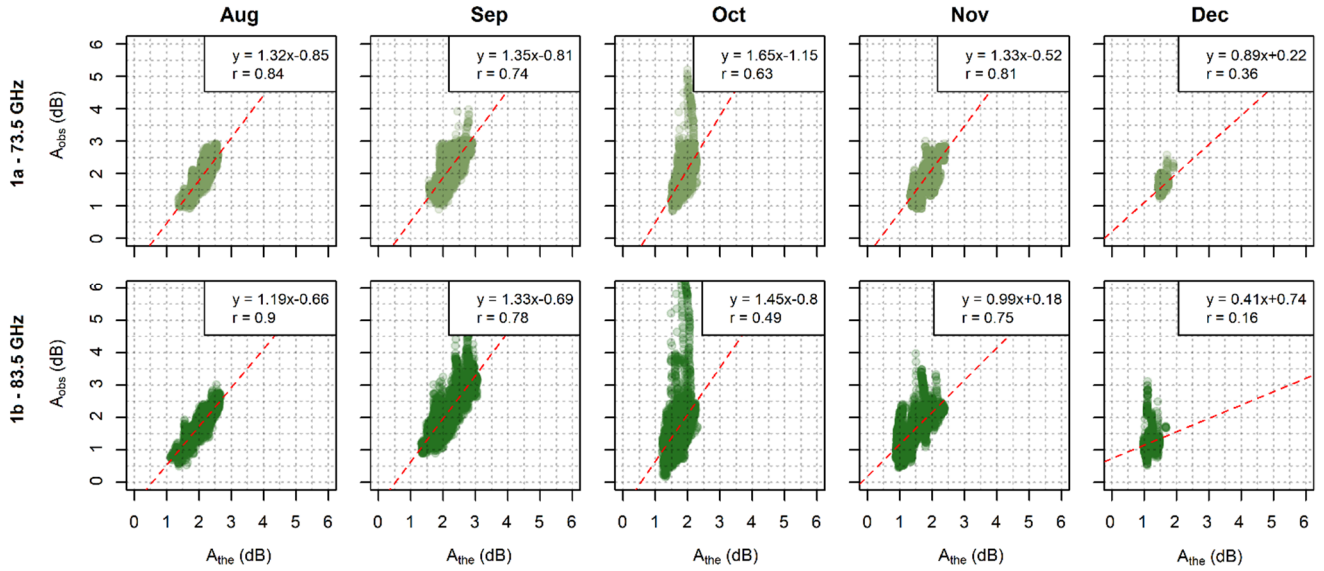
365 **Figure. 6: Comparison of theoretical (x-axis) and observed (y-axis) gas attenuations at the 73.5 and 83.5 GHz sub-links of the CML 1 for 5-min data. Data are shown separately for each month.**

4.2 Accuracy of the k-R power-law approximation

Evaluation of theoretical DSD: The relationship between attenuation and rainfall can be, for both frequencies, extremely well approximated by the power-law model, however, the parameters heavily depend on DSD (Fig. 7). For example, the

370 specific attenuation 16 dB km^{-1} corresponds to a rainfall intensity of about 30 mm h^{-1} for rainfall with DSD typical for stratiform rainfalls. However, throughout convective rainfall the same specific attenuation would occur for rainfall intensities of about 50 mm h^{-1}. For both frequencies the model using ITU parameter results between curves fitted to the rainfalls with stratiform resp. convective DSD. However, it is closer to the 'stratiform' curve for lower rainfall intensities and approximates a better 'convective' curve for intensities higher than approx. 10–15 mm h^{-1}. The ITU parameters, therefore, provide a good

375 approximation when no information on precipitation type is available.

Evaluation on Duebendorf DSD data: Similar power-law fits are obtained when modeling attenuation and rainfall from real DSD observations. Here, two types of rainfall are classified based on mass-weighted drop diameter D_m (Eq. 10). The fitting of the classification threshold $\widehat{D_m}$ (Eq. 11) results in parameters $c = 1.29$ h^{-d} mm$^{1/d}$ and $d = 0.16$. The relation between rainfall intensity and theoretical attenuation obtained is shown, together with fitted k-R power-law curves, in Fig. 8. The spread of

380 rainfall intensity clearly grows with increasing attenuation. The k-R model deficiencies, therefore, increase with increasing rainfall intensity, as can be also seen from the RMSE values (Table 4).
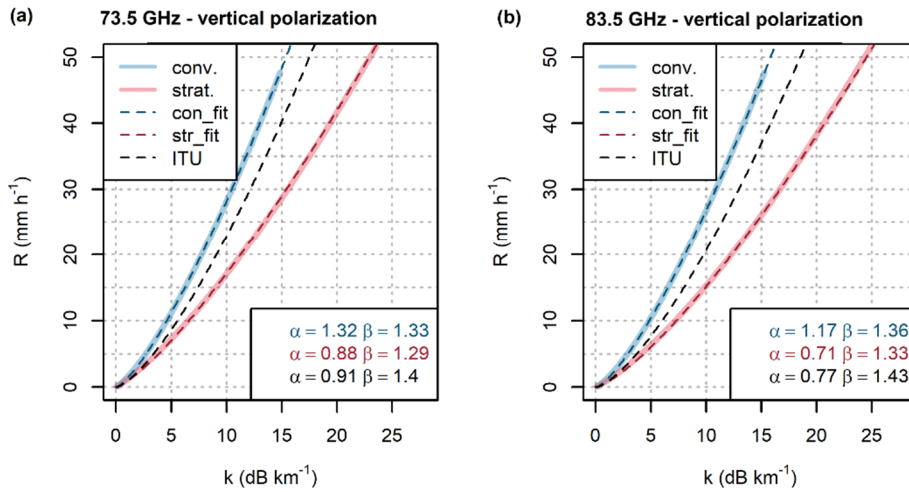
Figure 7: Attenuation-rainfall relation for vertically polarized radio waves at (a) frequency 73.5 GHz and (b) 83.5 GHz derived from theoretical DSD corresponding to stratiform and convective rainfall. A k-R model (Eq. 8) with parameters according to ITU-R (2005) lies between the curves corresponding to virtual convective and stratiform rainfalls. Parameters of the models are shown.
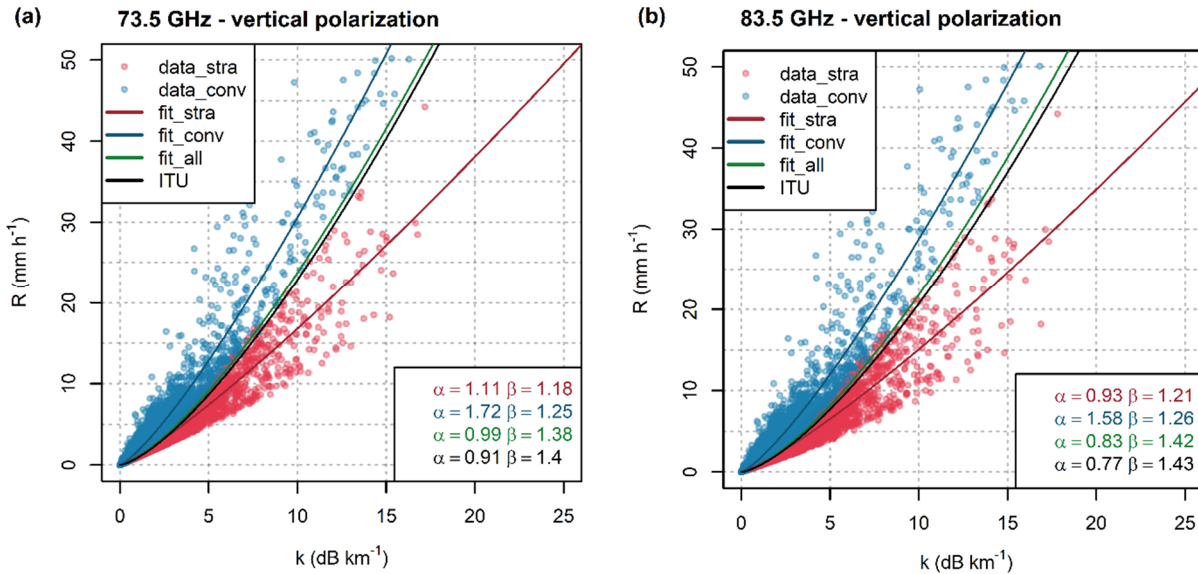
Figure 8: Relation between specific attenuation and rainfall derived from one year of DSD data for vertically polarized radio waves at (a) frequency 73.5 GHz, and (b) 83.5 GHz. The k-R model (Eq. 8) with parameters according to ITU-R (2005) resembles the model optimized for all the records. The curves optimized for convective and stratiform rainfalls differ significantly. Parameters of the models are shown.

Table 4: RMSE values measuring differences between observed and simulated rainfall using the k-R model with different parameter sets. The evaluation is provided separately for light, moderate, and heavy rainfall as well as for the whole dataset.

Parameter set	Freq. (GHz)	RMSE (mm h⁻¹)			
		All data	*Light rainfall R ≤ 4*	*Moderate rainfall R = 4–12*	*Heavy rainfall R > 12*
Separate fit	73.5	0.67	0.20	1.34	4.75
	83.5	0.73	0.24	1.48	5.08
Joined fit	73.5	1.17	0.43	2.46	8.03
	83.5	1.26	0.41	2.73	8.43
ITU	73.5	1.18	0.41	2.39	8.17
	83.5	1.27	0.45	2.63	8.74

4.3 Wet antenna attenuation

Figure 9 presents CML data at a 1-min temporal resolution featuring: i) attenuation during peak rainfall; ii) attenuation during dry spells at night on 3rd Nov. and after the rainfall; and iii) attenuations during dew occurrence on the morning of 4th Nov. Attenuation during peak rainfall is markedly influenced by raindrop path attenuation and is proportional to path length (Fig. 9b). In contrast, attenuation both during dry spells and after a rainfall, as well as attenuation during dew occurrences (with the exception of sub-link 6b) is dominated by WAA and, thus, independent of path length. Therefore, the WAA quantification method utilizing different CML path lengths (section 3.5) seems to be conceptually justified.
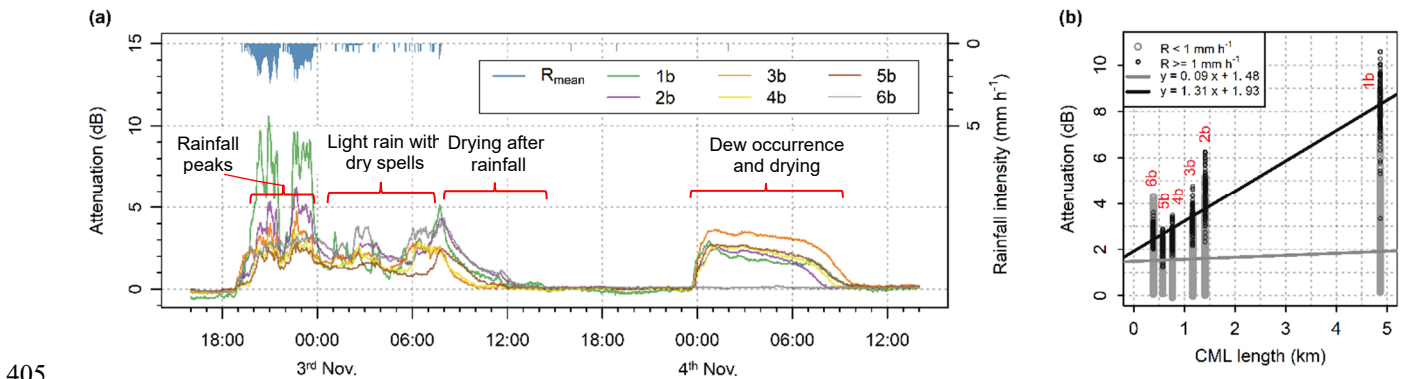
Figure 9: (a) Total rainfall-induced attenuation of 83–84 GHz sub-links and mean rainfall intensity from all four rain gauges. Period with peak rainfalls on 2nd Nov. from approx. 19:00 to 00:00, period with light rainfall and dry spells on 3rd Nov. from approx. 00:00 to 05:00, antenna drying period on 3rd Nov. from approx. 08:00 to 14:00, and dew occurrence and subsequent antenna drying on 4th Nov. from approx. 00:00 to 10:00. (b) Total attenuation plotted against path length for 83-84 GHz sub-links with two separate linear fits for intervals with moderate rainfall and intervals with very-light rainfall including dry spells. Period from 19:00 on 2nd Nov. to 14:00 on 3rd Nov. is shown.
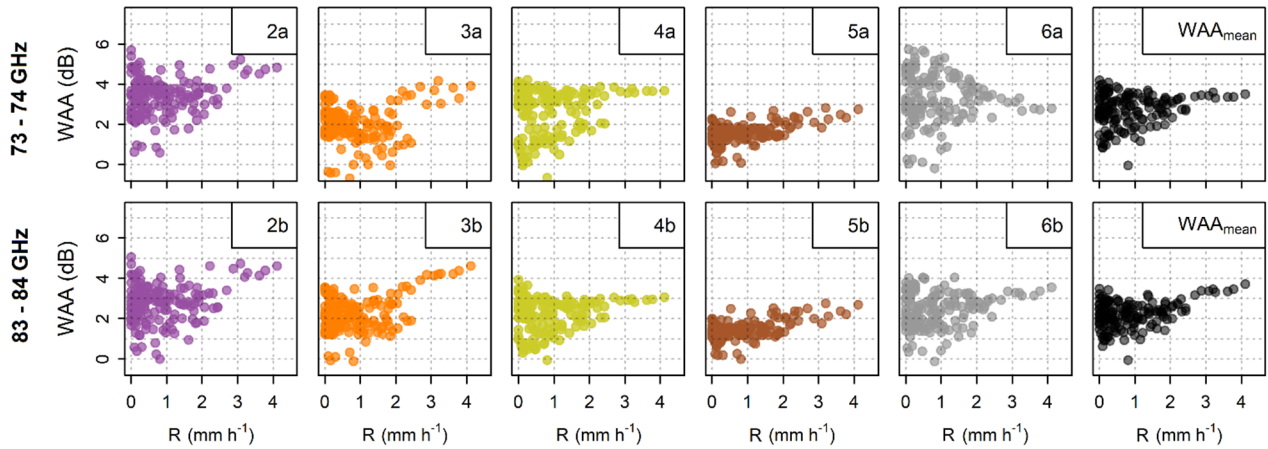
Figure 10: Wet antenna attenuation during rainfall estimated from the differential attenuation of short and long CMLs. WAAs for both sub-links (73–74 GHz and 83–84 GHz) are shown for CML 1–5. The panels on the right side show mean WAA for all CMLs.

415   WAA quantified for each shorter CML and their average is shown in Fig. 10 at a 15-min temporal resolution. The correlation to rainfall intensity is weak except for sub-links 6a and 5b with correlation coefficients r = 0.46 and r = 0.53, respectively. Higher rainfall intensities are, in general, associated with high WAA, whereas WAA reaches a wide range of values during lower intensities. WAA averaged over the whole evaluation period is between 1.60–3.47 dB for the 73–74 GHz sub-links and 1.41–2.48 for the 83–84 GHz sub-links. Further, inspection of CML time series reveals that attenuation after rainfall decreases

420   exponentially which is probably due to the drying of the antennas (Fig. 9a, 3rd Nov).

WAA also contributes to total attenuation during the occurrence of dew when water condensates on the antenna radomes. Attenuation associated with dew deposition is similar for both frequency bands and reaches up to 4 dB (Fig. 9a, 4th Nov morning). These values are higher than WAA caused by rainfall.

4.4 Rainfall estimation

425   Figure 11 shows QPEs obtained from CMLs using the k-R model with ITU parameters and parameters derived from DSD during rainfalls classified as stratiform. Note that DSD is obtained from the independent Duebendorf dataset. The long CML, in particular the 83.5 GHz sub-link, is capable of capturing even light rainfall intensities reliably. The correlation to rain-gauge observations is excellent (r ≈ 0.96). However, QPEs derived with ITU parameters tend to underestimate light rainfalls, which also leads to increased RMSE (Table 5). The model with DSD-derived parameters improves performance with respect to all

430   metrics. Sub-link 1a also remains significantly underestimated with DSD-derived parameters. This is due to deficits in the baseline and WAA identification. The underestimation is pronounced especially during very light rainfalls with rainfall intensities under 1 mm h^{-1}, which represent 25 % of total rainfall depth. Shorter CMLs are less sensitive to rainfall along their shorter path and are more affected by deficiencies in the estimated baseline and WAA. Thus, use of DSD parameters does not significantly improve performance of short CMLs. CMLs shorter than 1 km overestimate rainfall intensities more than longer

435   CMLs.
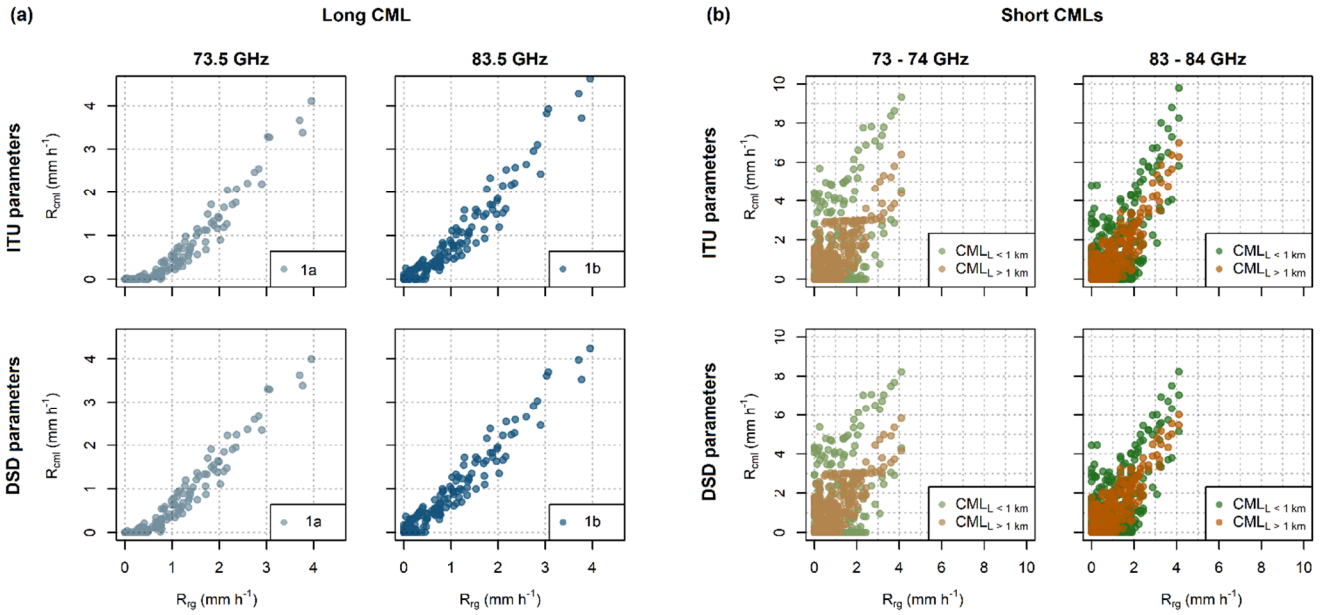
Figure 11: CML QPEs for the long CML (a) and short (b) CMLs when using k-R model with ITU (top) and DSD-derived (bottom) parameters. Results are shown for both frequency ranges. QPEs for short CMLs are differentiated by color into two groups to depict CMLs with path lengths shorter and longer than 1 km separately.

440 **Table 5: Performance metrics of the CML QPEs obtained with the k-R model using ITU and DSD-derived parameters**

Sub-link	ITU parameters			DSD parameters		
	r	rel.	RMSE	r	rel.	RMSE
id	(-)	error (-)	(mm h^{-1})	(-)	error (-)	(mm h^{-1})
1a	0.95	-0.44	0.49	0.96	-0.35	0.39
1b	0.96	-0.17	0.31	0.97	-0.08	0.24
2a	0.86	0.10	0.64	0.86	0.23	0.64
2b	0.87	0.26	0.75	0.87	0.33	0.69
3a	0.67	0.34	0.92	0.66	0.43	0.97
3b	0.84	0.15	0.71	0.83	0.21	0.69
4a	0.74	-0.48	0.95	0.74	-0.44	0.92
4b	0.78	0.24	1.31	0.77	0.26	1.14
5a	0.73	-0.78	0.92	0.74	-0.77	0.90
5b	0.80	-0.61	0.79	0.81	-0.59	0.76
6a	0.57	1.26	2.29	0.53	1.25	2.18
6b	0.63	0.61	1.56	0.61	0.59	1.44

In general, rainfall retrieval by E-band CMLs is affected during light rainfalls not only by deficiencies related to WAA and the baseline, but also deficiencies related to DSD. WAA and baseline-related errors clearly dominate by shorter CMLs, whereas regarding the 4.86-km-long CML, DSD seems to have a similar or even larger effect (in the case of the 83.5 GHz sub-link).
445 The effect of DSD is likely to increase with high rainfall intensities, which were, however, not encountered during the case study period.

5   Discussion

Gaseous attenuation: The theoretical gaseous attenuation for 73.5 GHz sub-link ranges between 1.33 dB and 2.90 dB (amplitude 0.33 dB km^{-1}) and for the 83.5 GHz sub-link between 0.95 dB and 3.06 dB (amplitude 0.45 dB km^{-1}). These
450 fluctuations have a minor effect on rainfall retrieval (with respect to uncaptured baseline variability), as 0.33, resp. 0.45 dB km^{-1} corresponds to a rainfall intensity of about 0.19 mm h^{-1} resp. 0.25 mm h^{-1} for 73.5 GHz and 83.5 GHz sub-links. On the other hand, this signal is sufficiently strong to enable the detection of water vapor at long CMLs, as 0.33 dB km^{-1} and 0.45 dB km^{-1} corresponds by the long CML (4.86 km) of 1.60 dB resp. 2.19 dB. The major challenge lies in the separation of gaseous attenuation from losses caused by other phenomena. This is easier during periods without rainfall, nevertheless, the
455 following causes of losses need to be identified and separated.

First, WAA occurring after rainfall and during dew events can reach 4 dB, *i.e.*, substantially exceeds the gaseous attenuation. Here, a safety window of 6 h size was used before and after each rain gauge tipping to exclude periods with WAA contribution. This mostly eliminated WAA before and after rainfall events and WAA during strong dew events causing a rain-gauge tip. However, such eliminations considerably reduce ratio of time intervals with observations. Moreover, periods before and after
460 rainfalls might have higher relative humidity than average and discarding those from the evaluation leads to potentially biased long-term estimates of water vapor density.

Second, signal fluctuations due to multipath propagation or other sources of uncertainty might affect the observed attenuation level. Multipath interferences often lead to a decreased signal power level of one sub-link while keeping the signal power level of the other sub-link (Valtr et al., 2011).
465 Finally, hardware related artifacts might destroy a gaseous attenuation signal. For example, sub-link 6a drifts about 1.5 dB during the period from the end of October to mid-December. This drift is clearly related to the hardware as the total loss due to gaseous attenuation along the path length of 0.39 km can reach only about 0.13 dB. Such a drift would, however, make the quantification of gaseous attenuation impossible even at long CMLs.

The separation of gaseous attenuation from other sources of signal loss is challenging. Further research could take advantage
470 of the 10 GHz duplex separation between the sub-links of E-band CMLs. Combining attenuation information from CMLs of different lengths might also be promising.

Accuracy of the k-R power law approximation: The relation between rainfall and raindrop attenuation (Eq. 7 and 8) on E-band frequencies is substantially more dependent on DSD than on 15–40 GHz CMLs (Chwala, 2017). The parameters of

the power-law model (Eq. 8), when optimized for all the DSD data, corresponds extremely well to the ITU parameters (ITU-R, 2005). However, high values of RMSE results from the variability in DSD when using one fit for all the records. Separate fits for convective and stratiform rainfalls halve the RMSE values. Moreover, the separate power-law fits are closer to linear (parameter β between 1.18 and 1.26, compared to β between 1.38 and 1.4) and are less prone to errors related to non-uniform rainfall distribution along the CML path. Errors due to non-linearity of Eq. (8) might be reduced by reconstructing rainfall spatial variability along the CML path from the neighboring CMLs, or by introducing a climate-based relation between the non-uniformity of rainfall distribution and rainfall intensity. Such methods will, however, require further research. In general, unknown DSD will probably be one of the major uncertainties in quantitative estimates of heavy rainfall. On the other hand, high sensitivity to DSD creates the opportunity to infer information on DSD from the attenuation of E-band CMLs, *e.g.*, in a condensed form of DSD moments. This is, in theory, also possible at 15–40 GHz, though difficult to accomplish in practice (Leth et al., 2019). Additional information on rainfall intensity or a combination with attenuation data of CMLs operating at lower frequencies will be required for DSD retrieval.

Quality check before rainfall retrieval: Quality check was performed through visually inspecting time series of total losses. In the case of CML 2 a sudden change in baseline by 2 dB was manually corrected. More details to hardware related artifacts is provided in *Appendix B*.

Dry-wet weather classification and baseline separation:

The dry-wet classification has been reported as an important step in CML pre-processing as it minimizes unwanted changes in attenuation level by setting the baseline separately for each event from the relatively short period before the event (Chwala and Kunstmann, 2019; Overeem et al., 2011). Here, dry-wet weather classification was not used for baseline identification. It was a pragmatic choice enabling better descriptions of the WAA effect. Dry-wet classification is also needed for filtering out periods with increased attenuation due to WAA (after rainfall and during dew events), nevertheless, these periods are in the event-based evaluation not included.

The separation of wet weather (including dew occurrence) was identified as a crucial step when analyzing attenuation due to water vapor. When rain gauges are not available a CML-based classification needs to be performed. The dry-wet weather classification (Schleiss and Berne, 2010) used in *Appendix A* is designed to identify rainy periods and consider dew occurrences as dry weather. Although sensitivity to dew events can be increased by optimizing the parameters of the algorithm, dew events have similar dynamics as changes in air humidity as they are both dependent on temperature. Thus, other methods also considering observations of neighboring CMLs (Overeem et al., 2011) might be more appropriate for the dry-wet weather classification used for the separation of attenuation caused by water vapor.

The baseline identification method with a moving median (without dry-wet weather classification) performed well for rainfall retrieval purposes. It should be noted that, with the exception of one case, the observed attenuation levels were stable. The median moving window baseline with window size of one week was capable to correct long-term drift, which occurred on sub-link 6a (*Appendix B*). Window size of one week is sufficiently long to not include more than 50 % of wet weather records into the window at any time step in the temperate climate. However, the median moving window baseline is not suitable for

distinguishing between long-term drift related to hardware malfunction (*e.g.*, sub-link 6a) and drift related to seasonal changes in air humidity and temperature (sub-links 1a and 1b). Constant baseline was, therefore, used for analysis of gaseous attenuation on sub-links 1a and 1b instead. Possible water vapor monitoring thus poses higher requirements on the hardware with respect to the stability of the attenuation baseline.

Wet antenna attenuation: Quantification of WAA during rainfall is based on the assumption that rainfall has a uniform distribution over the study area, and that water formation on the surface of antenna radomes is the same for both the short CMLs and the long one. In our case, the first assumption holds well as all four rain gauges observe similar rainfall intensities during the evaluated events. The correlation coefficient between rain gauges at sites 1, 2 and 4, which are closer to each other, is 0.94–0.96 and 0.88–0.93 for the more distant rain gauge at site 3. The similarity in antenna characteristics, *i.e.* hydrophobic properties of antenna radomes as well as their actual status, was not inspected directly. That said, the estimation procedure is relatively insensitive to WAA occurring on the long CML as attenuation along its path dominates over WAA, even during relatively light rainfalls and, thus, WAA does not significantly influence the estimated specific attenuation (13).

WAA during rainfall is weakly correlated to rainfall intensity (*e.g.*, Schleiss et al., 2013). Our results are limited to light and moderate rainfall only. Schleiss et al. (2013) reported drying of up to six hours with an exponential decrease of WAA, which also corresponds well to our observations (Fig. 9a). However, quantification of exact durations of drying require additional instrumentation to enable us to determine ends of rainfalls directly. The exponential WAA decrease during drying was also reported by Leth et al. (2018) who suggested that this drying pattern occurs on antennas with non-degraded coating, which is also the case of the CML antennas analyzed. On the other hand, WAA attenuation patterns on antennas with degraded coating might be markedly different.

WAA due to water vapor condensation reaches higher values than during light rainfall. This might be caused by an absence of water rivulets (Leth et al., 2018). The higher values of attenuation caused by water droplets, in comparison to attenuation caused by rivulets, was also reported by Mancini et al. (2019). Comparable attenuation patterns of light rainfall and water vapor condensation may cause the misclassification of dew as rainfall.

In general, WAA quantified in this study is slightly higher than WAA reported for lower frequencies (Leth et al., 2018). However, the relative contribution of WAA to the total attenuation is less significant (given the high sensitivity of CMLs to raindrop path attenuation). WAA is, thus, a smaller source of possible bias than on 15–40 GHz frequencies, nevertheless, its accurate quantification is still important, especially for shorter CMLs. In addition, WAA during heavy rainfalls was not investigated in this study and might be higher, as was shown for lower frequencies by Fencl et al. (2019).

Rainfall estimation: The E-band CMLs proved to be markedly more sensitive to raindrop path attenuation than 15–40 GHz devices. The long CML provided surprisingly accurate rainfall estimates, even for light rainfalls lower than 1 mm h^{-1} in intensity (Fig. 11). Assuming a detection threshold of 1 dB (typical *tx* power quantization of older devices), a 1-km-long 83 GHz CML can already detect rainfall intensity of 0.6–1 mm h^{-1} depending on rainfall type, whereas, *e.g.*, a 23 GHz or 38 GHz CML only detects rainfalls heavier than 8.4 resp. 3.6 mm h^{-1}, *i.e.,* the sensitivity to light rainfalls is almost an order of

magnitude higher for E-band CMLs. Moreover, the quantization of *rx* and *tx* records has improved to 0.1 dB with E-band CMLs. On the other hand, long E-band CMLs are prone to outages (*rx* drops under detection level) during heavy rainfall. This high sensitivity to rainfall, together with improved quantization, opens the opportunity for monitoring rainfall with CMLs having a sub-kilometer path length, which was practically not possible before without adjusting CML QPEs to the rain gauges

545 (Fencl et al., 2017). Short CMLs are more affected by errors related to WAA, yet the influence of WAA is relatively smaller during heavier rainfall, which, however, did not occur during the evaluation period. The use of short CMLs may be convenient, especially during heavy rainfalls associated with high spatial variability by which an assumption about uniform rainfall distribution along a CML path is more likely valid than for long CMLs. Reliable rainfall estimation from short CMLs, however, requires further research on WAA modeling at E-band frequencies.

550 **Limitations of this study:** The study investigates the weather monitoring capabilities of E-band CMLs on a dataset comprised of four months of attenuation data from six Ericsson MINILINK CMLs operated within cellular backhaul. The number of CMLs and length of the period is sufficient to demonstrate the challenges and opportunities related to rainfall and water vapor monitoring at an E-band. However, the limited size of the dataset does not enable us to draw strong conclusions on the overall reliability of weather monitoring with an E-band, nor to investigate in detail new opportunities related to CML sensitivity to

555 water vapor and DSD.

Specifically, the dataset does not include heavy rainfalls. The reliability of E-band CML rainfall estimation for heavy rainfalls is based only on the evaluation of theoretical attenuations obtained from DSD observations (Duebendorf). The DSD effect on the attenuation-rainfall relation could not be, therefore, studied in detail on the observed CML data. Finally, air temperature and humidity are measured at two locations close to one node of the CML path. Despite these limitations, we believe that the

560 presented results reliably demonstrate new challenges and opportunities of E-band CML weather monitoring.

6   Conclusions

E-band microwave links are increasingly updating and frequently replacing the older hardware of backhaul networks operating mostly at 15–40 GHz. This investigation demonstrates new challenges and opportunities related to CML weather monitoring. The principles behind weather retrieval is the same as for lower frequency bands, nevertheless the influence of atmospheric

565 phenomena such as drop size distribution, or changes in air temperature and humidity affect radiowave propagation in a significantly different manner. Furthermore, hardware used by E-bands is different (quantization, accuracy, antenna wetting, etc.). The results, obtained from simulations and the case study with attenuation data from real-world CMLs, are encouraging. The main conclusions are listed below:

- E-band CMLs are markedly more attenuated by raindrops along their path than older 15–40 GHz devices, during

570 lighter rainfalls by about 20 times more than 15 GHz and 2 - 3 times more than 40 GHz devices. This significantly improves the ability of E-band CMLs to quantify rainfall intensity accurately during light rainfalls.

- The rainfall retrieval at E-band frequencies is less influenced by wet antenna attenuation than at lower frequencies. WAA observed in this study has a similar pattern as that described by Schleiss et al. (2013), *i.e.*, it is almost

uncorrelated with rainfall intensity and exhibits an exponential decrease after rainfall lasting up to several hours. WAA during dew occurrences reaches up to 4 dB.

- The power-law approximation of the attenuation-rainfall relation depends substantially more on DSD than on 15–40 GHz frequencies. The variability in DSD represents significant uncertainties in E-band CML rainfall retrieval. Use of different parameter sets for different types of rainfall, as done with weather radars, reduce DSD-related errors, nevertheless this requires additional information on rainfall type.

- The k-R relation at E-band frequencies is less linear than at lower frequencies. This might cause errors, especially by longer CMLs, for which a uniform distribution of rainfall intensity along their path cannot always be assumed. On the other hand, even short (sub-kilometer) E-band CMLs are sufficiently sensitive to raindrop path attenuation to be used for rainfall retrieval.

- Gaseous attenuation at E-band CMLs is detectable, however, it is substantially smaller than attenuation due to rainfall. Fluctuations in specific attenuation caused by water vapor typically not exceed 1 dB km^{-1} in the region of temperate climate. This magnitude is reached by rainfall with intensity around 1 mm h^{-1}. Gaseous attenuation is driven mainly by water vapor density and is, thus, in theory, an accurate predictor of this atmospheric variable. This, however, requires the efficient separation of attenuation from other signal losses which is, in practice, challenging. Our first results show that this separation is, to some extent, possible during dry weather periods, if a sufficiently long CML (several km) is available.

In general, the ongoing shift of CML networks towards higher frequencies creates opportunities for the monitoring of rainfall on a qualitatively different level. New E-band CMLs are able to observe light rainfalls and, in combination with lower frequency CMLs, potentially serve as DSD predictors. The rainfall retrieval methods developed for CMLs operating at 15–40 GHz frequencies proved to be useful for E-band CMLs as well. Water vapor retrieval from E-band CMLs having a path length of several kilometers might be possible, although the efficient separation of gaseous attenuation from other signal losses will be challenging in practice. This first experience with E-band CML weather retrieval, as presented in this study, will hopefully contribute to more robust designs of future experimental studies and case studies investigating this new technology with respect to weather monitoring.

Appendix A – Dry-wet weather classification

The classification is performed separately for each sub-link on quality-checked total observed losses. The algorithm of Schleiss and Berne (2010) is used which is based on a moving window standard deviation. The window size is set to 15 minutes and the threshold for classifying the record as wet (σ_0) is set to the 94 % quantile of all standard deviations resulting from the moving window filter. The 94 % probability corresponds approximately to the wet weather ratio in the Prague data as classified by the rain gauges.
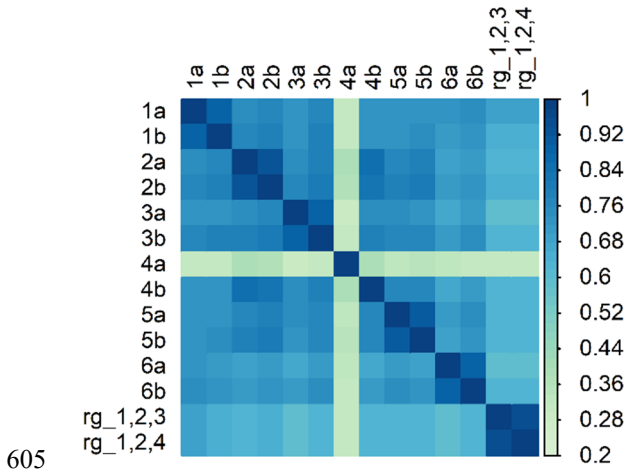
Figure A1: Statistical relationship between dry-wet classifiers based on single CML sub-links and rain gauges along the path of the long CML (rg_1,2,3) and three rain gauges near five shorter CMLs (rg_1,2,4) expressed by correlation coefficient.

Dry-wet weather classifiers obtained from CML sub-links are compared with each other and with classifiers obtained from rain gauge observations. Correlation is used here as a measure of similarity. The evaluation of dry-wet weather is performed on one-minute data because precise identification of the onset and ending of rainfall significantly affects baseline identification methods based on dry wet classification, as well as the quantification of wet antenna attenuation.

Dry-wet weather classifiers of single sub-links belonging to one CML are strongly correlated (Fig. A1). An exception is sub-link 4a which is affected by a hardware malfunction (*Appendix B*). The correlation between the classifiers of sub-links belonging to different CMLs is lower but still reaches high values ranging between $r = 0.57$ and $r = 0.84$. The correlation of CML classifiers to the classifiers based on rain gauges is, on average, slightly lower ($r = 0.57$–0.67).

The evaluation of dry-wet weather classification is only approximate because tipping bucket rain gauges are unable to detect the exact beginning or end of a rain event. Visual inspection of time series reveals that disagreement between rain gauges and CMLs occur most commonly during dew events and during periods of low temperature where mixed or snow events probably occur. Although sensitivity to dew events can be increased by optimizing the parameters of the algorithm, dew events have similar dynamics as changes in air humidity as they are both dependent on temperature. Thus, other methods also considering observations of neighboring CMLs (Overeem et al., 2011) might be more appropriate for the dry-wet weather classification used for the separation of attenuation caused by water vapor.

Appendix B – Hardware-related artifacts

There have been three types of hardware-related artifacts identified (visually) in the Prague data (Fig. B1): a) a sudden change in L_t, b) long-term gradual L_t drift, and c) 'degraded resolution'. 'Degraded resolution' is defined as behavior where *tx* and *rx* change with considerably lower frequency than is common with other CMLs. The degraded resolution can be easily recognized visually as a time series with no signal fluctuation within intervals of several hours.
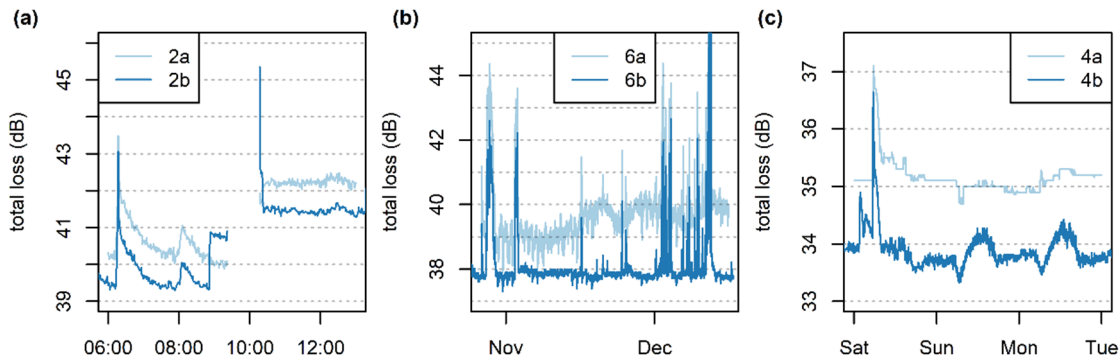
630 **Figure B1: Demonstration of hardware related artifacts (a) sudden change in the baseline of CML 2, (b) baseline drift of sub-link 6a and (c) degraded resolution of sub-link 4a.**

The sudden change in L_t of about 2 dB occurred on CML 2 on both sub-links (Fig. B1a). The change in baseline level was proceeded by approx. two hours of an outage. The long-term gradual drift of L_t occurred on sub-link 6a (Fig. B1b). L_t levels observed during dry weather increased gradually, on average, by about 1.5 dB during the experimental period. Finally, sub-

635 link 4a was affected during the whole experimental period by a degraded resolution (Fig. B1c). Interestingly, the degraded resolution was more pronounced during dry weather periods than rainy ones.

In general, attenuation levels during dry weather are relatively stable with respect to long-term drift (in the order of weeks). It holds for all CMLs except the 73 GHz sub-link of CML 6 which has dry weather attenuation levels of about 1.5 dB higher at the end of the period compared to the beginning (Fig. B1b). The most significant fluctuations in the baseline occur during dew

640 events when water film forming on the CML antennas causes wet antenna attenuation (section 4.3). The baseline fluctuations related to water vapor are presented in section 4.1 (Fig. 5).

The hardware related artifacts identified in the E-band attenuation time series are similar to those occurring on 15–40 GHz CMLs. The 'degraded resolution' can be identified easily by analyzing attenuation variability within (sub)hourly subsets. Detecting (and correcting for) the sudden change in attenuation level will be especially challenging in operation mode when

645 attenuation needs to be processed in real-time. Long-term drift can be captured very well and corrected using a median moving window with a size of one week. Such a size of window is sufficiently long to not include more than 50 % of wet weather records into the window at any time step in the temperate climate

Supplement link (will be included by Copernicus).

650

Code and data availability. The code for Prague data analysis and Prague data are publically available at Zenodo repository DOI 10.5281/zenodo.3632095. Duebendorf data (disdrometer observations) and the code are available upon request from the corresponding author.

Author contribution. MF and VB. designed the study layout. Data was collected by MF, VB and MD. Analysis was performed by MF with contribution of MD, MG, and PV. MF prepared the manuscript with contribution of all co-authors.

Competing interests. The authors declare that they have no conflict of interest.

Acknowledgements. This work was supported by the projects of Czech Science Foundation (GACR) No. 17-16389S and No. 20-14151J. We would like to thank T-Mobile Czech Republic a.s. for kindly providing us CML data and specifically to Pavel Kubík, for assisting with our numerous requests. Special thanks are extended to Prazska vodohospodarska spolecnost a.s. for providing rainfall data from their rain gauge network and Prazske vodovody a kanalizace, a.s. who carefully maintained the rain gauges. Last, but not least, we would like to thank Eawag for supporting COMMON project and Dr. Christian Chwala from Karlsruhe Institute of Technology (KIT) and University of Augsburg for supporting our analysis by calculating extinction cross-sections and providing Python implementation of Liebe model for calculating attenuation due to water vapor.

References

Atlas, D. and Ulbrich, C. W.: Path- and Area-Integrated Rainfall Measurement by Microwave Attenuation in the 1–3 cm Band, J. Appl. Meteor., 16(12), 1322–1331, doi:10.1175/1520-0450(1977)016<1322:PAAIRM>2.0.CO;2, 1977.

Berne, A. and Uijlenhoet, R.: Path-averaged rainfall estimation using microwave links: Uncertainty due to spatial rainfall variability, Geophys. Res. Lett., 34(7), L07403, doi:10.1029/2007GL029409, 2007.

Chwala, C.: Precipitation and humidity observation using a microwave transmission experiment and commercial microwave links, [online] Available from: https://opus.bibliothek.uni-augsburg.de/opus4/frontdoor/index/index/docId/37908 (Accessed 2 December 2019), 2017.

Chwala, C. and Kunstmann, H.: Commercial microwave link networks for rainfall observation: Assessment of the current status and future challenges, Wiley Interdisciplinary Reviews: Water, 6(2), e1337, doi:10.1002/wat2.1337, 2019.

Chwala, C., Keis, F. and Kunstmann, H.: Real-time data acquisition of commercial microwave link networks for hydrometeorological applications, Atmos. Meas. Tech., 9(3), 991–999, doi:10.5194/amt-9-991-2016, 2016.

David, N., Alpert, P. and Messer, H.: Technical Note: Novel method for water vapour monitoring using wireless communication networks measurements, Atmospheric Chemistry and Physics, 9(7), 2413–2418, doi:https://doi.org/10.5194/acp-9-2413-2009, 2009.

Ericsson: Ericsson Microwave Outlook, [online] Available from: https://www.ericsson.com/assets/local/microwave-outlook/documents/ericsson-microwave-outlook-report-2016.pdf (Accessed 15 July 2017), 2016.

Ericsson: Ericsson Microwave Outlook Report - 2018, [online] Available from: https://www.ericsson.com/en/reports-and-papers/microwave-outlook/reports/2018 (Accessed 10 December 2019), 2018.

Ericsson: Ericsson Microwave Outlook Report - 2019, [online] Available from: https://www.ericsson.com/en/reports-and-papers/microwave-outlook/reports/2019 (Accessed 10 December 2019), 2019.

Fencl, M., Dohnal, M., Rieckermann, J. and Bareš, V.: Gauge-adjusted rainfall estimates from commercial microwave links, Hydrol. Earth Syst. Sci., 21(1), 617–634, doi:10.5194/hess-21-617-2017, 2017.

690 Fencl, M., Valtr, P., Kvičera, M. and Bareš, V.: Quantifying Wet Antenna Attenuation in 38-GHz Commercial Microwave Links of Cellular Backhaul, IEEE Geoscience and Remote Sensing Letters, 16(4), 514–518, doi:10.1109/LGRS.2018.2876696, 2019.

Fencl, M., Dohnal, M. and Bareš, V.: Raw and preprocessed data for the paper Atmospheric Observations with E-band Microwave Links – Challenges and Opportunities, , doi:10.5281/zenodo.3632095, 2020.

695 Fujiwara, M.: Raindrop-size Distribution from Individual Storms, J. Atmos. Sci., 22(5), 585–591, doi:10.1175/1520-0469(1965)022<0585:RSDFIS>2.0.CO;2, 1965.

Hansryd, J., Li, Y., Chen, J. and Ligander, P.: Long term path attenuation measurement of the 71–76 GHz band in a 70/80 GHz microwave link, in Proceedings of the Fourth European Conference on Antennas and Propagation, pp. 1–4., 2010.

Hong, E. S., Lane, S., Murrell, D., Tarasenko, N. and Christodoulou, C.: Mitigation of Reflector Dish Wet Antenna Effect at 700 72 and 84 GHz, IEEE Antennas and Wireless Propagation Letters, 16, 3100–3103, doi:10.1109/LAWP.2017.2762519, 2017.

Humphrey, M. D., Istok, J. D., Lee, J. Y., Hevesi, J. A. and Flint, A. L.: A New Method for Automated Dynamic Calibration of Tipping-Bucket Rain Gauges, J. Atmos. Oceanic Technol., 14(6), 1513–1519, doi:10.1175/1520-0426(1997)014<1513:ANMFAD>2.0.CO;2, 1997.

Internationale Fernmelde-Union, Ed.: Handbook radiowave propagation information for desining terrestrial point-to-point 705 links, Ed. 2008., ITU, Geneva., 2009.

ITU-R: ITU-R P.838-3, [online] Available from: http://www.itu.int/dms_pubrec/itu-r/rec/p/R-REC-P.838-3-200503-I!!PDF-E.pdf, 2005.

ITU-R: RECOMMENDATION ITU-R P.676-12 - Attenuation by atmospheric gases and related effects, [online] Available from: https://www.itu.int/dms_pubrec/itu-r/rec/p/R-REC-P.676-12-201908-I!!PDF-E.pdf, 2019.

710 Jaffrain, J. and Berne, A.: Experimental Quantification of the Sampling Uncertainty Associated with Measurements from PARSIVEL Disdrometers, J. Hydrometeor., 12(3), 352–370, doi:10.1175/2010JHM1244.1, 2010.

Jaffrain, J. and Berne, A.: Quantification of the Small-Scale Spatial Structure of the Raindrop Size Distribution from a Network of Disdrometers, J. Appl. Meteor. Climatol., 51(5), 941–953, doi:10.1175/JAMC-D-11-0136.1, 2012.

Leijnse, H., Uijlenhoet, R. and Stricker, J. N. M.: Rainfall measurement using radio links from cellular communication 715 networks, Water Resour. Res., 43(3), W03201, doi:10.1029/2006WR005631, 2007.

Leijnse, H., Uijlenhoet, R. and Stricker, J. N. M.: Microwave link rainfall estimation: Effects of link length and frequency, temporal sampling, power resolution, and wet antenna attenuation, Advances in Water Resources, 31(11), 1481–1493, doi:10.1016/j.advwatres.2008.03.004, 2008.

Leth, T. C. van, Overeem, A., Leijnse, H. and Uijlenhoet, R.: A measurement campaign to assess sources of error in 720 microwave link rainfall estimation, Atmospheric Measurement Techniques, 11(8), 4645–4669, doi:https://doi.org/10.5194/amt-11-4645-2018, 2018.

Leth, T. C. van, Leijnse, H., Overeem, A. and Uijlenhoet, R.: Estimating raindrop size distributions using microwave link measurements, Atmospheric Measurement Techniques Discussions, 1–27, doi:https://doi.org/10.5194/amt-2019-51, 2019.

Liebe, H. J., Hufford, G. A. and Cotton, M. G.: Propagation modeling of moist air and suspended water/ice particles at frequencies below 1000 GHz. [online] Available from: http://adsabs.harvard.edu/abs/1993apet.agar.....L (Accessed 17 October 2019), 1993.

Luini, L., Roveda, G., Zaffaroni, M., Costa, M. and Riva, C.: EM wave propagation experiment at E band and D band for 5G wireless systems: Preliminary results, in 12th European Conference on Antennas and Propagation (EuCAP 2018), pp. 1–5., 2018.

Mancini, A., Lebrón, R. M. and Salazar, J. L.: The Impact of a Wet S-Band Radome on Dual-Polarized Phased-Array Radar System Performance, IEEE Transactions on Antennas and Propagation, 67(1), 207–220, doi:10.1109/TAP.2018.2876733, 2019.

Messer, H., Zinevich, A. and Alpert, P.: Environmental Monitoring by Wireless Communication Networks, Science, 312(5774), 713–713, doi:10.1126/science.1120034, 2006.

Minda, H. and Nakamura, K.: High Temporal Resolution Path-Average Rain Gauge with 50-GHz Band Microwave, Journal of Atmospheric and Oceanic Technology, 22(2), 165–179, doi:10.1175/JTECH-1683.1, 2005.

Mishchenko, M. I. and Travis, L. D.: Capabilities and limitations of a current FORTRAN implementation of the T-matrix method for randomly oriented, rotationally symmetric scatterers, Journal of Quantitative Spectroscopy and Radiative Transfer, 60(3), 309–324, 1998.

Ostrometzky, J., Raich, R., Bao, L., Hansryd, J. and Messer, H.: The Wet-Antenna Effect—A Factor to be Considered in Future Communication Networks, IEEE Transactions on Antennas and Propagation, 66(1), 315–322, doi:10.1109/TAP.2017.2767620, 2018.

Overeem, A., Leijnse, H. and Uijlenhoet, R.: Measuring urban rainfall using microwave links from commercial cellular communication networks, Water Resources Research, 47(12), doi:10.1029/2010WR010350, 2011.

Schleiss, M. and Berne, A.: Identification of Dry and Rainy Periods Using Telecommunication Microwave Links, IEEE Geoscience and Remote Sensing Letters, 7(3), 611–615, doi:10.1109/LGRS.2010.2043052, 2010.

Schleiss, M., Rieckermann, J. and Berne, A.: Quantification and Modeling of Wet-Antenna Attenuation for Commercial Microwave Links, IEEE Geoscience and Remote Sensing Letters, 10(5), 1195–1199, doi:10.1109/LGRS.2012.2236074, 2013.

Ulbrich, C. W.: Natural Variations in the Analytical Form of the Raindrop Size Distribution, J. Climate Appl. Meteor., 22(10), 1764–1775, doi:10.1175/1520-0450(1983)022<1764:NVITAF>2.0.CO;2, 1983.

Valtr, P., Pechac, P., Kvicera, V. and Grabner, M.: Estimation of the Refractivity Structure of the Lower Troposphere From Measurements on a Terrestrial Multiple-Receiver Radio Link, IEEE Transactions on Antennas and Propagation, 59(5), 1707–1715, doi:10.1109/TAP.2011.2122234, 2011.

Wang, Z., Schleiss, M., Jaffrain, J., Berne, A. and Rieckermann, J.: Using Markov switching models to infer dry and rainy periods from telecommunication microwave link signals, Atmospheric Measurement Techniques, 5(7), 1847–1859, doi:10.5194/amt-5-1847-2012, 2012.

Woodhouse, I. H.: Introduction to microwave remote sensing, CRC press., 2017.